Electrical Engineering
https://doi.org/10.1007/s00202-023-01990-5

ORIGINAL PAPER

Eccentricity fault detection in synchronous reluctance machines

Hossein Hooshmandi Safa[1] · **Hossein Abootorabi Zarchi**[1]

Received: 10 June 2023 / Accepted: 12 August 2023

Abstract
This paper introduces a novel index for static eccentricity (SE) fault diagnosis in synchronous reluctance motors (SynRMs). Although SynRMs with rotor barriers under SE have been modeled in a few papers, any indices for the fault detection have not yet been reported. The proposed index is a specific frequency pattern in the motor current, which can also determine the fault severity. A novel analytical magnetic field investigation is applied to ascertain the proposed index. An accurate nonlinear numerical method is proposed for the motor inductances calculation. The model considers the rotor flux barriers, magnetic saturation, and the stator slots effect. The air gap flux density and the motor current are then achieved. The fast Fourier transform is exploited as a signal-processing tool to calculate motor current spectra. Then, a two-dimension time-stepping finite element method is used to attest of the proposed numerical model. Effectiveness of the proposed index is verified by simulation and experimental tests.

Keywords Modified winding function · Finite element model · Synchronous reluctance motors · Static eccentricity · Motor current analysis

1 Introduction

Synchronous reluctance machines (SynRMs) have recently achieved extensive interest due to their high torque, speed, and efficiency [1]. The torque production in SynRMs is based on the magnetic reluctance theory. The stator in a SynRM is like an induction machine (IM), and the rotor is constructed of laminated silicon content steel. The flux barriers are distributed in each pole to increase the saliency ratio.

There are some electrical and mechanical faults in the electrical machines. Static eccentricity (SE) is one of the typical mechanical faults in electrical machines. In SE, the rotor axis and the rotation axis are shifted from the stator axis while coinciding with each other. Eccentricity inclines to intensify the produced electromagnetic force on the rotor. The different approaches have been reported in the literature for the SE fault diagnosis in electrical machines. In [2], the amplitude of sideband components (ASBCs) with a specific pattern extracted from the stator current spectrum has been used as an index for eccentricity fault diagnosis in permanent magnet synchronous motors (PMSMs).

In [3], the peak-to-peak amplitude of the induced voltage in the winding wound around the stator teeth has been used for eccentricity diagnosis in PMSMs. However, the index only detects the dynamic eccentricity (DE), because SE does not affect the amplitude of the corresponding induced voltage in the search winding. In [4], the amplitude of the fifth and seventh harmonic of stator current have been used for static eccentricity diagnosis in a PMSM. In [5], using the Vd and Vq voltages, a method has been proposed for identifying the rotor faults due to the manufacturing and assembly failures in axial flux permanent magnet synchronous motors. The change of the point in the Vd–Vq plane is used as a fault indicator. In order to indicate type of the fault and its severity, the shift direction and the amount of the shift have been exploited, respectively. The force distribution, vibration, and acoustic noise are used in [6] to investigate the partial demagnetization and static eccentricity effect on PMSMs. The field reconstruction method has been exploited for force analysis.

In [7], motor current signature analysis (MCSA) with DSP-based signal-processing system has been used for fault diagnosis in induction motors. The slip is estimated by the Bayesian method. Then, a search algorithm is used to identify the associated fault frequency. In [8], the resolver signals used

✉ Hossein Abootorabi Zarchi
abootorabi@um.ac.ir

Hossein Hooshmandi Safa
hossein.hooshmandi@mail.um.ac.ir

[1] Electrical Engineering Department, Faculty of Engineering, Ferdowsi University of Mashhad, Mashhad, Iran

Published online: 07 October 2023

for position estimation have been used for eccentricity fault diagnosis in inverter-driven electrical machines. The winding function method (WFM) has been used for the modeling. Then, the simulation results have been verified by FEM and experimental tests. However, the position sensor has been removed in the new control schemes of electrical motors [9]. Therefore, the proposed method in [8] cannot be used generally in motor drive systems.

In [10], an index based on processing developed torque using the time series data mining method has been introduced to detect eccentricity in round rotor synchronous motors. The magnitude of the 17th and 19th harmonic components have been used for fault analysis. In [11], the triple harmonics in the line current spectrum has been proposed for the SE fault diagnosis in a salient pole synchronous motor without flux barriers with rotor bars. In [12], the torque ripple has been used as an index to investigate the eccentricity fault in a salient pole synchronous reluctance motor (without flux barriers). It has been claimed that SE and DE do not induce any component in the current spectrum of the motor. However, the results achieved from the proposed model have not been verified by experimental tests.

Although the eccentricity faults in PMSMs [13–18], IMs [19–21], and synchronous machines [10–12] are exhaustively scrutinized, there are limited works on eccentric SynRMs. The existing research has only been conducted on eccentricity modeling, and no indices for SE detection in SynRMs with distributed rotor flux barriers have been reported so far. For example, in [22], a magnetic equivalent circuit (MEC) has been used to predict the torque and force in eccentric SynRM. However, an approximated air gap function is used in the model; therefore, it is not accurate enough to detect SE. Moreover, the nonlinear features of core materials, stator slots, and saturation effects have been ignored. In [23], an improved MEC model has been proposed to analyze the magnetic field density, unbalanced magnetic force, and torque in eccentric SynRMs. In the model, the iron saturation and slotting effect have been considered. However, a current supply is used as an input that cannot be exploited in MCSA. Moreover, no index has been proposed to detect eccentricity in SynRMs. In [24], a SynRM has been characterized analytically using WFM. Nevertheless, the air gap modeling in an eccentric machine has not been discussed.

According to the above review, there is still no index to diagnose eccentricity fault in SynRMs with distributed flux barriers. The first main novelty of this paper is to propose an index for the fast and accurate diagnosis of SE fault in SynRMs. The proposed index can be used for the motors with any winding layout, rotor flux barrier configuration, and output power.

A rapid numerical method based on the modified winding function is developed to calculate the magnetic field and torque in the concentric and eccentric SynRMs. In this model, the geometric specifications of the motor and saturation effect are considered. This model can be used in the preliminary machine design procedure. Moreover, the proposed model is a fast simulation tool to derive an appropriate index for the fault diagnosis systems of SynRMs. The effectiveness of the proposed model and SE fault diagnosis index is validated by FEM and experimental tests.

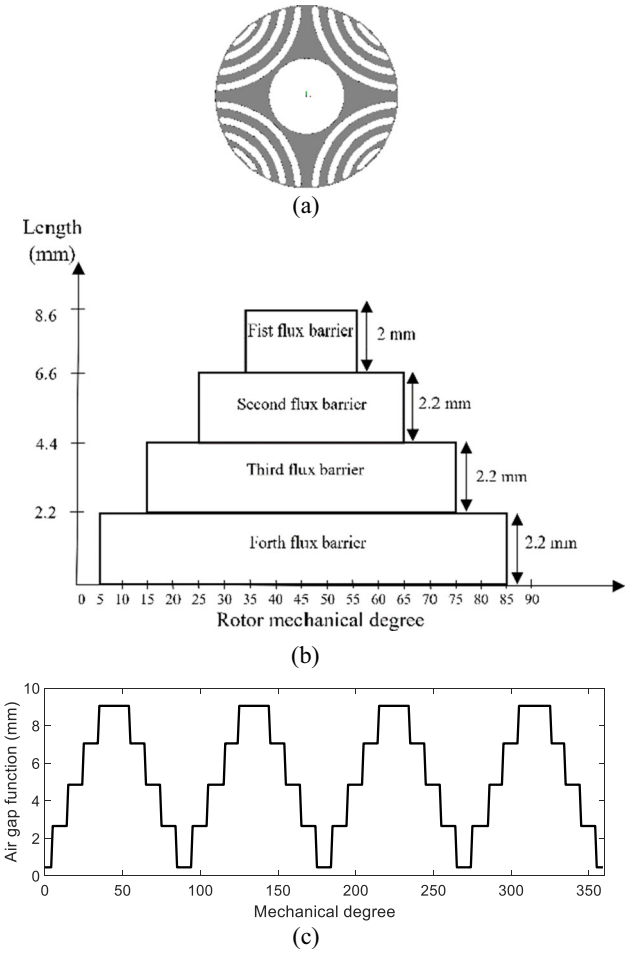

Fig. 1 **a** cross-section of the rotor **b** the flux barriers length **c** the air gap function

2 Theoretical analysis of air gap field for the pattern identification

Analyzing the motor performance under eccentricity demands accurate air gap modeling. The flux barriers in SynRMs cause the magnetic reluctance of the rotor to vary. The rotor reluctance can be modeled using the definition of the rotor position-dependent air gap function. In this section, firstly, based on the number of flux barriers and their width, the air gap function of the healthy motor is modeled. Then SE is added to the air gap function. Figure 1 demonstrates

cross-section of the rotor, the individual air gap lengths for each flux barrier, and the calculated air gap function, respectively. In this model, the circular flux barriers with constant wide are used. The mechanical air gap length is added to the overall air gap length obtained from the flux barriers.

As can be seen in Fig. 1c, the period of the air gap function is $T = 2\pi$. The air gap function can be written in the form of the Fourier series as follows:

$$g_{rel}(\varphi, \theta_r) = a_0 + \sum_{n=1}^{N}\left(a_n \cos\left(\frac{2\pi}{T} n\theta_r - \varphi\right) + b_n \sin\left(\frac{2\pi}{T} n\theta_r - \varphi\right)\right) \tag{1}$$

where g_{rel} is the effective air gap length related to flux barriers, φ is the angular position in the stator reference frame, θ_r is rotor angular position, and a_0, a_n, and b_n are Fourier coefficients which can be obtained as follows:

$$a_0 = \frac{1}{T}\int_T g(\varphi, \theta_r) d\theta_r \tag{2}$$

$$a_n = \frac{2}{T}\int_T g(\varphi, \theta_r) \cos\left(\frac{2\pi}{T} n\theta_r - \varphi\right) d\theta_r \tag{3}$$

$$b_n = \frac{2}{T}\int_T g(\varphi, \theta_r) \sin\left(\frac{2\pi}{T} n\theta_r - \varphi\right) d\theta_r \tag{4}$$

Since is even, the coefficients b_n are equal to zero;$b_n = 0$. Considering the first term of a_n, and substituting $T = 2\pi$, (1) can be simplified as follows:

$$g_{textrel}(\varphi, \theta_r) = a_0 + a_1 \cos(\theta_r - \varphi) = a_0\left(1 + \frac{a_1}{a_0}\cos(\theta_r - \varphi)\right) \tag{5}$$

With assuming $k_1 = -\frac{a_1}{a_0}$, (1) is rewritten as follows:

$$g_{rel}(\varphi, \theta_r) = a_0(1 - k_1 \cos(\theta_r - \varphi)) \tag{6}$$

The permeance function, which is the inverse of the air gap function, is calculated by

$$\sigma(\varphi, \theta_r) = \frac{1}{g_{rel}(\varphi, \theta_r)} = \frac{1}{a_0(1 - k_1\cos(\theta_r - \varphi))} = \frac{1}{a_0}\left(1 + k_1\cos(\theta_r - \varphi) + \frac{(k_1\cos(\theta_r - \varphi))^2}{2!} + \frac{(k_1\cos(\theta_r - \varphi))^3}{3!} + \ldots\right) \tag{7}$$

Because of the smaller values of the third and the higher terms of the above Eq. (7) can be reduced to

$$\sigma(\varphi, \theta_r) = \frac{1}{a_0}(1 + k_1\cos(\theta_r - \varphi)) \tag{8}$$

In (8),$\theta_r = \omega_r t = \frac{\omega_s}{P} t$; P is the pole pair number, and ω_s is the angular frequency of the supply. Therefore,

$$\sigma(\varphi, t) = \frac{1}{a_0}\left(1 + k_1\cos\left(\frac{\omega_s}{P} t - \varphi\right)\right) \tag{9}$$

The air gap flux density can be calculated as follows:

$$B_s(\varphi, t) = \sigma(\varphi, t)\int \mu_0 j_s(\varphi, t) d\varphi \tag{10}$$

where j_s is current density, which is defined as follows:

$$j_s(\varphi, t) = J_s \sin(\omega_s t - P\varphi) \tag{11}$$

Inserting (9) and (11) into (10) results in:

$$B_s(\varphi, t) = \frac{1}{a_0}\left(1 + k_1\cos\left(\frac{\omega_s}{P} t - \varphi\right)\right)\int \mu_0 J_s \sin(\omega_s t - P\varphi) d\varphi \tag{12}$$

By some simplification,B_s can be expressed as follows:

$$B_s(\varphi, t) = \frac{\mu_0 J_s}{a_0 P}\cos(\omega_s t - P\varphi) + \frac{\mu_0 J_s k_1}{2a_0 P}\left[\mathrm{Cos}\left(\left(1 + \frac{1}{P}\right)\omega_s t\right) - (P+1)\varphi + \mathrm{Cos}\left(\left(1 - \frac{1}{P}\right)\omega_s t\right) - (P-1)\varphi\right] \tag{13}$$

According to (13), in addition to the fundamental frequency in B_s, there are the side band components $\left(1 \pm \frac{1}{P}\right) f_s$. These components are produced in the healthy motor because the air gap length in SynRMs is not constant and depends on the rotor position. However, the amplitude of these sideband components is small in healthy conditions. It can easily be shown that by considering the higher order of a_n and repeating (6)–(13), the frequency pattern that appeared in the air gap flux density is as follows:

$$f = \left(1 \pm \frac{m}{P}\right) f_s \tag{14}$$

where m is a positive integer number, and f_s is the supply frequency. The air gap function in the SE case can be derived as follows.

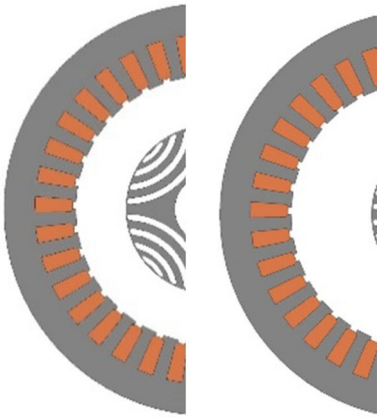

(a) (b)

Fig. 2 Cross-section of motor **a** healthy motor **b** motor with SE

$$g(\varphi, \theta_r) = g_{rel}(\varphi, \theta_r) - \delta_{se}\cos(\varphi) \tag{15}$$

where δ_{se} is SE degree and represented by (16)

$$\delta_{se} = \frac{\left|\overrightarrow{O_S O_W}\right|}{g_0} \tag{16}$$

Figure 2 shows the stator and the rotor position in the SE condition. O_s, O_r, and O_w are axes of the stator, rotor, and rotation axes, respectively. Using a similar procedure shown above for the SE case, it can be illustrated that B_s consists of the $\left(1 \pm \frac{m}{P}\right) f_s$ in the SE condition. The eccentricity increases the ASBCs rather than a healthy motor. Due to the flux linkage, which circulates in the stator windings, the back electromotive force is induced in each stator winding, which in turn produces the following current in the windings. Therefore, the stator current spectrum is an appropriate index for diagnosing of SE fault.

3 Dynamic simulation of SynRM

The dynamical model of the motor can be developed using the proposed rotor model. For energizing the stator winding, a three-phase sinusoidal voltage is used. The stator voltage is defined by:

$$\begin{bmatrix} v_a \\ v_b \\ v_c \end{bmatrix} = \begin{bmatrix} R_s & 0 & 0 \\ 0 & R_s & 0 \\ 0 & 0 & R_s \end{bmatrix} \begin{bmatrix} i_a \\ i_b \\ i_c \end{bmatrix} + \begin{bmatrix} \frac{d\psi_a}{dt} \\ \frac{d\psi_b}{dt} \\ \frac{d\psi_c}{dt} \end{bmatrix} \tag{17}$$

where v, R_s, and i are the voltage, resistance, and current of each stator winding, respectively. φ is the individual flux linkage as follows:

$$\begin{bmatrix} \psi_a \\ \psi_b \\ \psi_c \end{bmatrix} = \begin{bmatrix} L_{aa} & L_{ab} & L_{ac} \\ L_{ba} & L_{bb} & L_{bc} \\ L_{ca} & L_{cb} & L_{cc} \end{bmatrix} \begin{bmatrix} i_a \\ i_b \\ i_c \end{bmatrix} \tag{18}$$

Using the co-energy method, the electromagnetic torque can be calculated for any rotor position as follows:

$$T_e = \frac{1}{2}[I]^T \left[\frac{\partial L(\theta_r)}{\partial \theta_r}\right][I] \tag{19}$$

$[I]$ is the stator current matrix, and L is the stator inductance matrix. The electro-mechanical equation of the motor is:

$$T_e - T_L = J\frac{d\omega_r}{dt} \tag{20}$$

where T_e is electromagnetic torque, T_L is load torque, and j and w_r are the inertia moment and the angular velocity of the rotor, respectively. Based on (19), to solve the dynamic simulation of the motor, the stator inductances are needed.

4 Stator inductance calculation

The WFM is achieved by exploiting the coupled electromagnetic equations. To consider eccentricity in WFM, the modified winding function method (MWFM) has been developed in [25]. The MWFM for a coil is defined as follows:

$$M(\varphi, \theta_r) = n(\varphi) - \langle M(\theta_r)\rangle \tag{21}$$

where $n(\varphi)$ is the stator turn function, and $\langle M(\theta_r)\rangle$ is the modified winding function's average which is calculated as follows:

$$\langle M(\theta_r)\rangle = \frac{1}{2\pi\langle g^{-1}(\varphi, \theta_r)\rangle}\int_0^{2\pi} n(\varphi)g^{-1}(\varphi, \theta_r)d\varphi \tag{22}$$

where $\langle g^{-1}\rangle$ is the average of the inverse air gap shown as follows:

$$\left\langle g^{-1}(\varphi, \theta_r)\right\rangle = \frac{1}{2\pi}\int_0^{2\pi} g^{-1}(\varphi, \theta_r)d\varphi \tag{23}$$

The mutual inductance between phase A and phase B is represented as follows:

$$L_{AB}(\theta_r) = \mu_0 r\ell \int_0^{2\pi} n_A(\varphi)M_B(\varphi, \theta_r)g^{-1}(\varphi, \theta_r)d\varphi \tag{24}$$

Table 1 SynRM specifications

Power	350 W
Speed	1500 r/min
Stator pole number	4
Stator slots number	36
Number of flux barriers per pole	4
Air gap length	0.45 mm
Rotor diameter	94 mm
Stack length	50 mm

where μ is the magnetic permeability of air , r is the rotor outer radius, and is the stack length. As can be seen in (24), to calculate the inductance accurately, the air gap should be modeled precisely. The flux barriers and SE are modeled in section II. In this section, in order to improve the accuracy of the proposed model, the stator slots and the saturation effect are modeled. The stator slots are modeled as follows:

$$g(\varphi, \theta_r) = g_{\text{rel}} - \delta_{\text{Se}} \cos(\varphi) - \delta_{\text{slot}} \cos(N_s \varphi) \tag{25}$$

where δ_{slot} is the constant-coefficient related to the stator slots effect, and N_s is the number of stator slots. The magnetic permeability of the iron paths is decreased by saturation. Therefore, the reluctance of the area around the saturation is increased. In [26], the air gap length has been used to model the saturation. Therefore, instead of reducing the iron permeability, the air gap length can be used to model the saturation level. Therefore, the inverse air gap function is modified as follows:

$$g^{-1}(\varphi, \theta_r) = \frac{(1 - \delta_{\text{sat}} + \delta_{\text{sat}} \cos(2P(\omega_s t - \varphi))}{g_{\text{rel}}(\varphi, \theta_r) - \delta_{\text{se}} \cos(\varphi) - \delta_{\text{slot}} \cos(N_s \varphi)} \tag{26}$$

where δ_{sat} is the constant-coefficient related to the saturation effect, ω_s is the angular supply frequency, and P is the number of pole pairs. δ_{sat} is defined as follows [27]

$$\delta_{\text{sat}} = \frac{2(k_{\text{sat}} - 1)}{3k_{\text{sat}}} \tag{27}$$

k_{sat} Is the saturation factor, which is the ratio of the maximum flux density at the teeth region encompassing the air gap to that of the flux density at the beginning of saturation. k_{sat} is calculated by finite element analysis (FEA). The motor parameters are presented in Table 1. Figure 3 illustrates the self and mutual inductance of the stator for healthy motor and motor with 50% SE. It can be seen that the SE changes the values of the inductances.

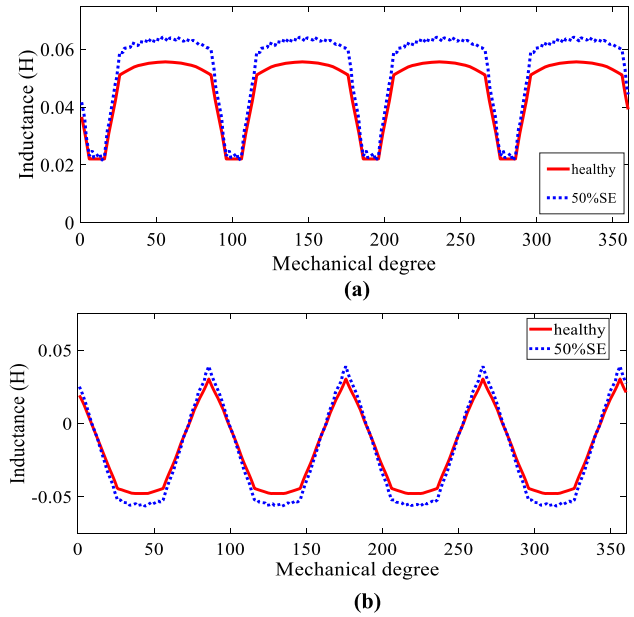

Fig. 3 **a** self-inductance for healthy motor **b** mutual inductance in 50% SE

5 Experimental set-up

The experimental set-up is illustrated in Fig. 4. The voltage source inverter is used. A crucial module within this drive system is powered by a Texas Instruments DIGITAL signal processor (DSP) known as the TMS320F28335. This high-performance processor plays a central role in ensuring the efficient operation and functionality of the entire system. This board serves as the crucial link between different modules within the drive system, responsible for relaying precise switching commands to the inverter boards. These commands are based on both the measured signals and the programmed control scheme. LEM LTS-6-NP current sensors and LEM LV-25-P voltage sensors are used in the inverter-fed drive system. An analog second-order low-pass filter is used to filter the current and voltage signals. The second-order low-pass filter is designed to attenuate or reduce the amplitude of high-frequency signals while allowing low-frequency components, which are essential for accurate and smooth motor control, to pass through unaffected. The filter achieves this by employing capacitors, resistors, and operational amplifiers in its circuitry.

Figure 4b provides a visual representation of the analog filter board. This board is responsible for adjusting the measured signals for the DSP board. This board has 10 analog inputs and 10 outputs. A second-order Butterworth analog filter stage is implemented on all inputs.

The low-pass filter circuit for voltage and current signals is illustrated in Fig. 4c. Notably, the filters' gain can be adjusted using the potentiometer on the board. The voltage gain of

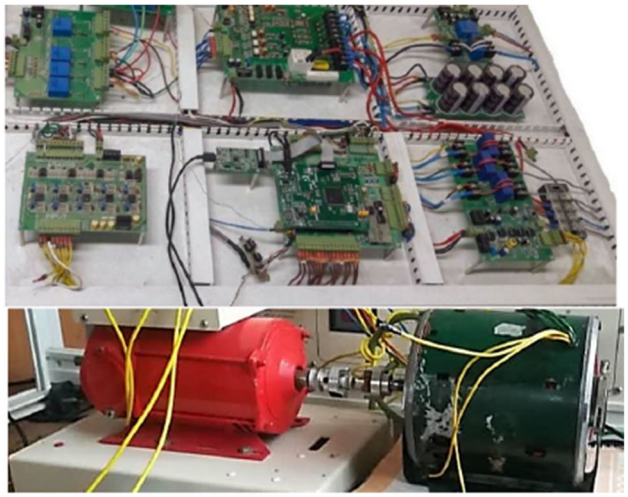

(a)

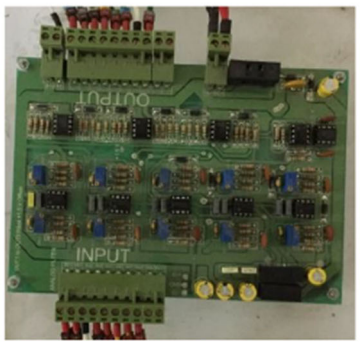

(b)

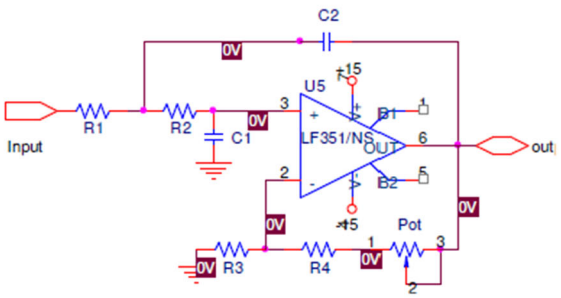

(c)

Fig. 4 **a** Experimental set-up **b** Analog Filter **c** Analog filter circuit

the amplifier and Butterworth filter can be calculated using Eq. (28).

$$Gain = 1 + \frac{R_4 + Pot}{R_3} \tag{28}$$

Table 2 presents the electrical parameters of each circuit component in Fig. 4c.

Inputs 1 to 6 of the analog filter board are additionally summed after filtering, using an offset voltage of + 1.5 V. To achieve proper signal alignment, particularly for the signals from the current sensor and the inverter phase voltage sensor, they must be connected to one of these inputs. This process ensures that the signals fall within the zero to V3 range before being fed into the ADC on the DSP board.

Table 2 Electrical parameters of filter circuit

R1	1.5 kΩ	C1	220 nF
R2	100Ω	C2	330 nF
R3	12 kΩ	Pot	10 kΩ
R4	0.1 kΩ		

The current sensors used in the drive system are used in the fault diagnosis system as well. The fast Fourier transform (FFT) is exploited as a signal-processing tool to calculate motor current spectra. A DC generator with a resistive load is used as the load of SynRM.

In order to create static eccentricity in the motor, the main bearings are replaced with the bearings with a smaller outer diameter, and the eccentric outer rings are used between the bearings and the housing. The value of eccentricity can be determined accurately by the machining of the outer rings.

6 Simulation and experimental results

In this paper, a SynRM under different static eccentricities is modeled. The dynamic model of motor is solved using the proposed model. The model is based on the MWFM considering the flux barriers. A 2D time-stepping FEM is used to verify the simulation results achieved from the proposed model. In FEM model, all physical complexities and nonlinearity of the motor are considered. The motor torque, flux density, current, and the current spectrum of the motor achieved from the proposed model have been compared with the FEM and experimental test results. The simulation and experimental results are obtained at the rated load and speed. Figure 5 shows the motor current in 50%SE. Figure 6a demonstrates the radial component of the air gap flux density distribution resulting from the proposed model for the healthy motor and motor with 50% SE. It can be seen that the SE distorts the distribution of the air gap flux density, which causes asymmetric current and torque. The comparison of the tangential and radial components of the air gap flux density obtained from the proposed model and FEM in 50%SE are depicted in Fig. 6b and c, respectively. The FEM results verify the accuracy of the proposed model. Figure 7a shows the simulation result for the electromagnetic torque for a healthy motor and motor with 50%SE in no-load conditions. Figure 7b compares the simulation and experimental results for the motor torque in 50%SE. Figure 8 illustrates the spectrum of the normalized line current obtained from

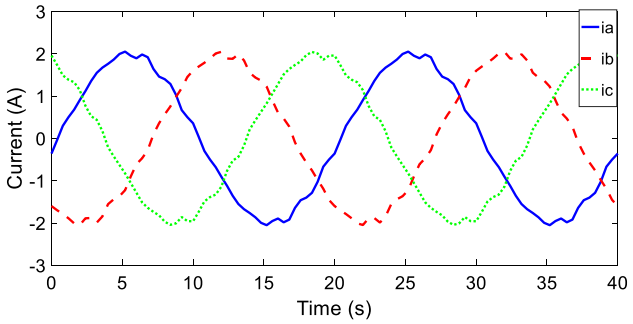

Fig. 5 Phase current waveforms (proposed model)

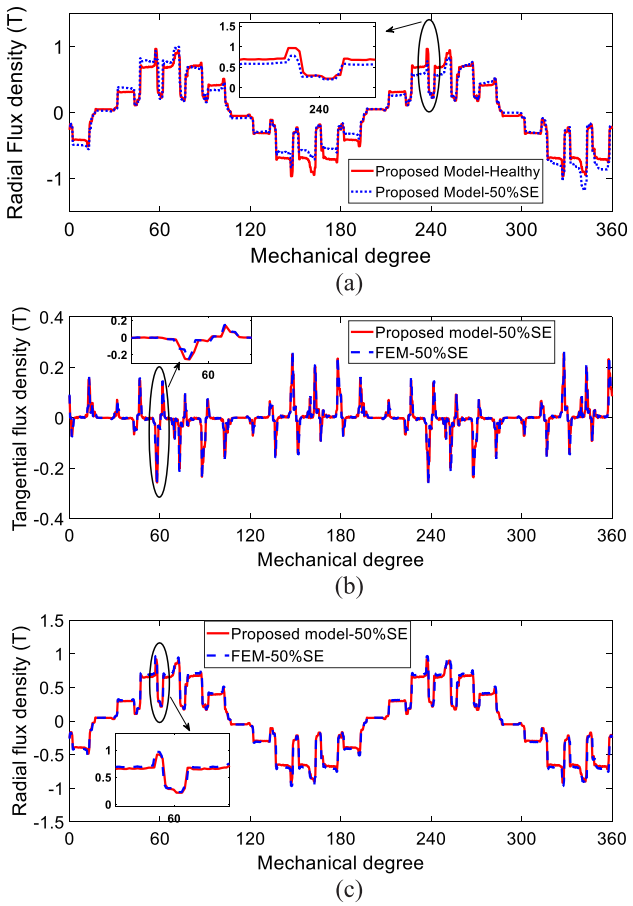

Fig. 6 Air gap flux density distribution **a** radial component for the healthy and faulty motor (proposed model) **b** comparison of the tangential component in 50%SE (proposed model and FEM) **c** comparison of the radial component in 50%SE (proposed model and FEM)

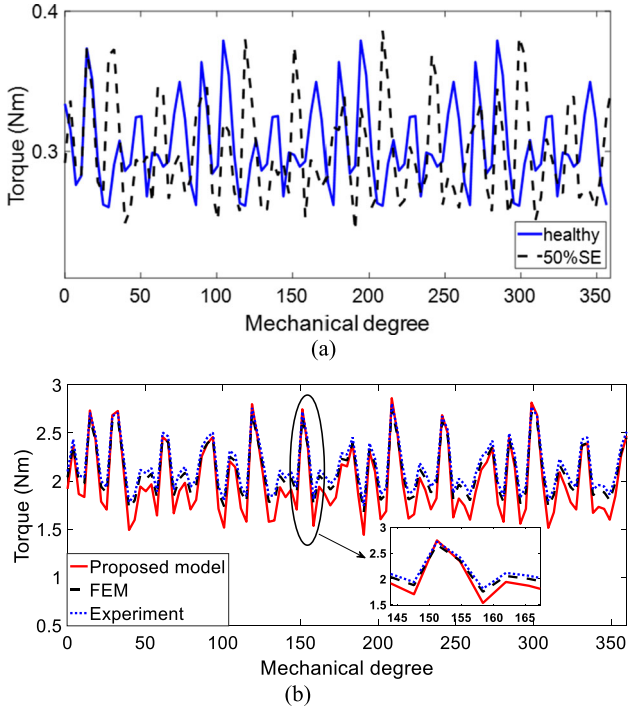

Fig. 7 **a** No load torque for healthy motor and motor with 50%SE **b** comparison of the torque in 50%SE

the proposed model for a healthy motor and motor with 30% and 50% SE, respectively.

Accordingly, the sideband components can be seen at $\left(1 \pm \frac{m}{P}\right) f_s$, as calculated in section II. This frequency pattern appears in the current spectrum of the healthy motor due to the flux barriers effect. However, the amplitude of the sideband components is raised with increasing in the SE fault degree. As can be seen in Fig. 8b, by increasing the SE to 30%, the amplitude of the sideband components of the stator current is increased at 25, 75, 100, and 125 Hz from −103.8, −105.7, −108.5, and −114.6 dB to −66.3, −64.9, −65.7, and −67.6 dB. Figure 8c demonstrates that by increasing the SE to 50%, the amplitude of the sideband components is increased to −49.2, −50.3, −49.4, and −51.6 dB. Figure 9 illustrates the spectrum of the normalized line current for a healthy motor and motor with 30% and 50% SE, obtained from the FEM. The spectrum of normalized line current achieved from experimental tests is shown in Fig. 10. The FEM and experimental test results verify the effectiveness of the introduced index in SE fault diagnosis of SynRMs. Figure 11 shows the variation of each sideband component at $\left(1 \pm \frac{m}{P}\right) f_s$ versus SE for the results obtained from the proposed model, FEM, and experimental tests. It can be.

Realized that the results of the proposed model are verified by the FEM and experiments. The ASBCs of the proposed index obtained from the simulations and the experimental tests are summarized in Table 3.

The impact of load level variation on this index has been thoroughly analyzed using FEM simulation for both a healthy motor and a motor experiencing various eccentricity levels.

Figure 12 illustrates the amplitude of $\left(1 - \frac{1}{P}\right) f_s$, ranging from the no-load condition to 120% rated load, and from 0% (representing a healthy motor) to 70% static eccentricity.

Table 3 Amplitude of the sideband components of the motor current spectra in different SE degree

	MWFM			FEM			Experimental		
	SE degree (%)								
Frequency (Hz)	0	30	50	0	30	50	0	30	50
25	−103.8	−66.3	−49.2	−105.2	−64.8	−51.6	−107.6	−67.9	−50.1
75	−105.7	−64.9	−50.3	−106.1	−63.2	−51.5	−108.5	−65.8	−50.4
100	−108.5	−65.7	−49.4	−109.2	−67.5	−57	−109.3	−68.7	−50.7
125	−114.6	−67.6	−51.6	−112.8	−66.3	−51	−110.6	−69.7	−51.3

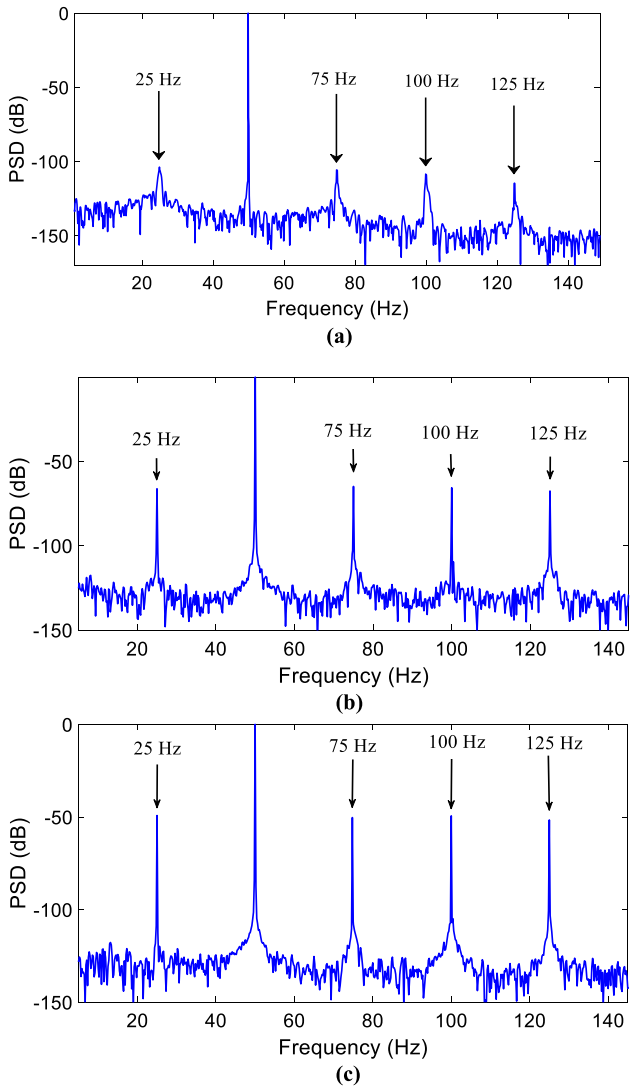

Fig. 8 Spectrum of normalized line current achieved from the proposed model tests **a** healthy motor **b** 30%SE **c** 50%SE

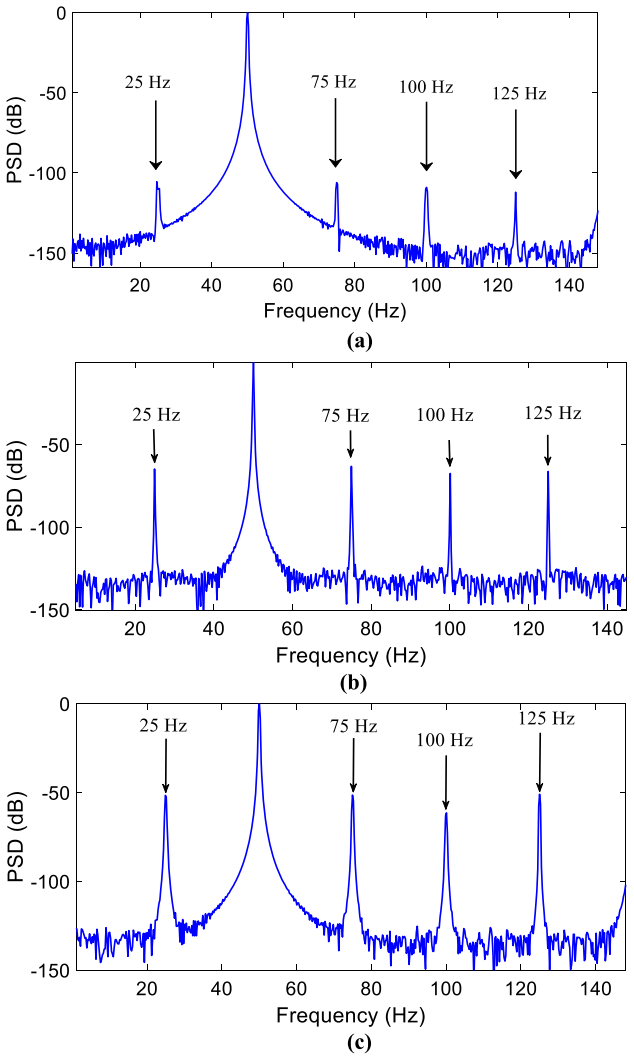

Fig. 9 Normalized line current spectra obtained from FEM **a** healthy motor **b** 30%SE **c** 50%SE

Notably, the results indicate that the load level has a negligible impact on the amplitude of the sideband components ASBCs. It is important to emphasize that the same findings hold true for the other sideband components of $\left(1 \pm \frac{m}{P}\right) f_s$.

It worth mentioning that the number of poles and supply frequency solely impact the frequency pattern. Furthermore, the demonstrated formula confirms that the Amplitude of Side Band Components (ASBCs) at these frequencies remains unaffected by load variations. Consequently, the

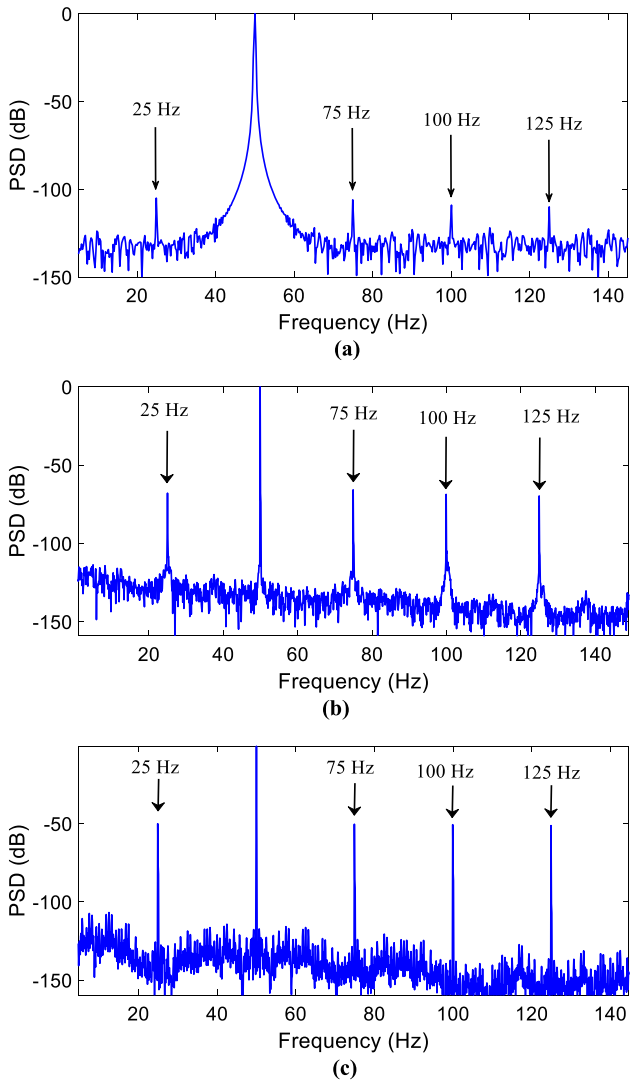

Fig. 10 Normalized line current spectra achieved from experimental tests **a** healthy motor **b** 30%SE **c** 50%SE

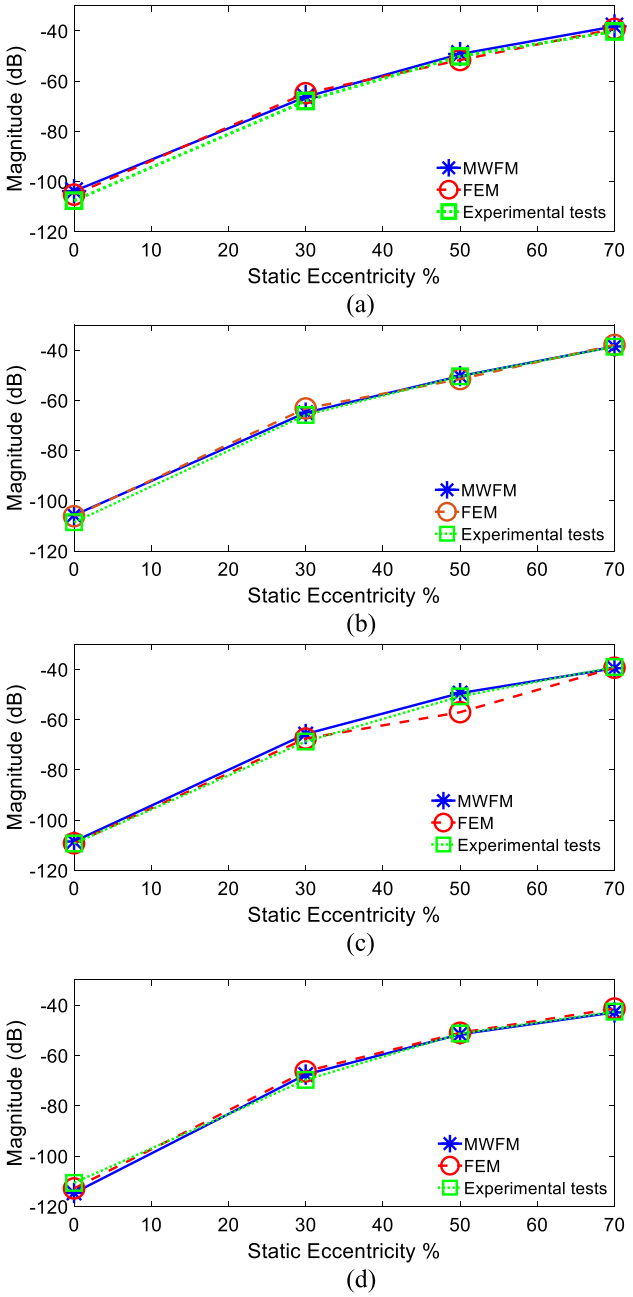

Fig. 11 Comparison of the ASBCs resulted from the proposed model, FEM, and experiments **a** 25Hz, **b** 75Hz, **c** 100Hz, **d** 125Hz

fault percentage emerges as the sole contributing factor that alters this index, underscoring its critical significance in fault diagnosis.

In order to examine the influence of the stator material on the generation of sideband components, the air core stator has been replaced with the original stator. Figure 13 presents the spectrum of the normalized line current obtained from the FEM model for a healthy motor, as well as motors with 30% and 50% static eccentricity (SE), respectively.

The sideband components at $\left(1 \pm \frac{1}{P}\right) f_s$ (25 Hz and 75 Hz) do not appear, even under the eccentricity conditions. This leads to the conclusion that the stator material and saturation play pivotal roles in the fault diagnosis process.

The results demonstrate the significance of considering the stator material and its saturation effects when evaluating and diagnosing faults in electric motors. This understanding can contribute to more accurate fault detection and effective maintenance strategies.

7 Conclusion

A fast and accurate numerical model has been proposed to calculate the motor inductances, air gap flux density, current, and torque. Then, a novel index based on the theoretical analysis has been introduced for static eccentricity fault diagnosis

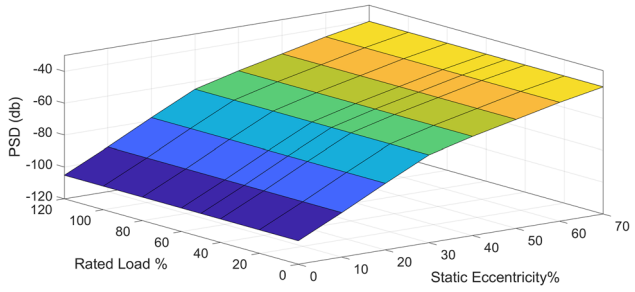

Fig. 12 Amplitude variation of sideband component versus load variation

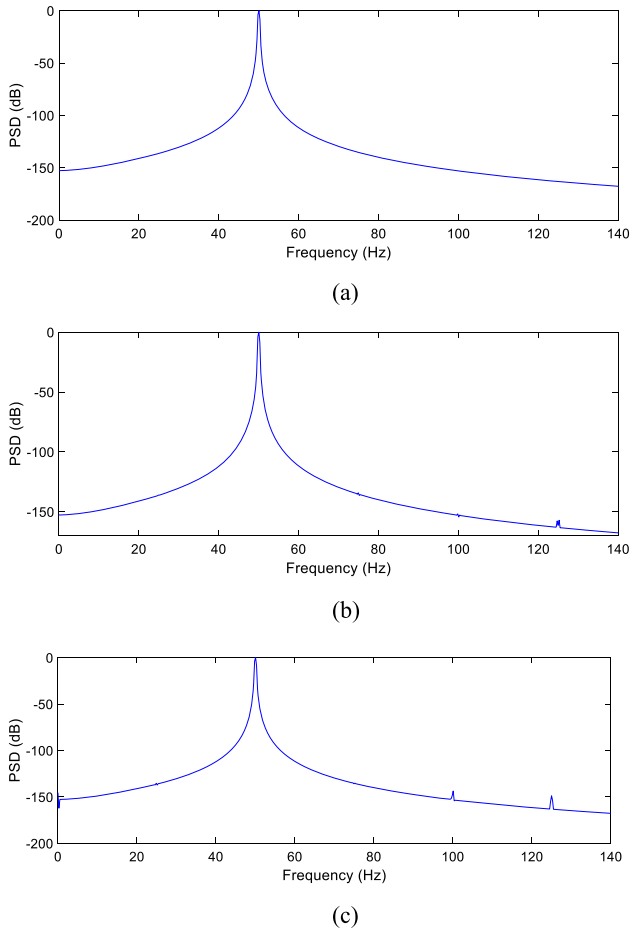

Fig. 13 The normalized line current spectra achieved from experimental tests **a** healthy motor **b** 30%SE **c** 50%SE

in SynRMs. The motor current was used as a proper signal for the fault detection system. The current spectrum was calculated using the FFT. It has been shown that the proposed frequency pattern exists in the spectrum of the healthy motor because of the flux barriers effect. Moreover, it has been illustrated that the amplitude of the sideband components was elevated with increasing the fault degree. In addition, the severity of the fault has been determined using the proposed index. Consequently, the proposed index can be used for SE fault diagnosis in SynRMs. Both FEM and experimental results have confirmed the effectiveness of the proposed index.

Authors' contributions Hossein Hooshmandi Safa wrote the main manuscript text and prepared the figures. All authors reviewed the manuscript.

Funding We declare that no funding was received for this research.

Declarations

Conflict of interest I declare that there is no competing financial or non-financial interest in relation to this work. The authors declare that they have no relation with a government agency that has a primary function other than research and education. Also, the authors declare that they are not an official representative or no behalf of the government.

References

1. Jurca N-F, Inţe RA, Popa D-C, Vărăticeanu B, Minciunescu P, Marţiş C (2021) Electromagnetic and mechanical analysis of a modular outer rotor synchronous reluctance machine for light propulsion vehicles. IEEE Trans Transp Electrif 7(4):2798–2811
2. Ebrahimi BM, Faiz J, Roshtkhari MJ (2009) Static-, dynamic-, and mixed-eccentricity fault diagnoses in permanent-magnet synchronous motors. IEEE Trans Ind Electron 56(11):4727–4739
3. Kang K, Song J, Kang C, Sung S, Jang G (2017) Real-time detection of the dynamic eccentricity in permanent-magnet synchronous motors by monitoring speed and back EMF induced in an additional winding. IEEE Trans Industr Electron 64(9):7191–7200
4. Haddad RZ, Strangas EG (2016) On the accuracy of fault detection and separation in permanent magnet synchronous machines using MCSA/MVSA and LDA. IEEE Trans Energy Convers 31(3):924–934
5. Haddad RZ (2020) Detection and identification of rotor faults in axial flux permanent magnet synchronous motors due to manufacturing and assembly imperfections. IEEE Trans Energy Convers 35(1):174–183
6. Torregrossa D, Khoobroo A, Fahimi B (2012) Prediction of acoustic noise and torque pulsation in PM synchronous machines with static eccentricity and partial demagnetization using field reconstruction method. IEEE Trans Ind Electron 59(2):934–944
7. Jung J-H, Lee J-J, Kwon B-H (2006) Online diagnosis of induction motors using MCSA. IEEE Trans Ind Electron 53(6):1842–1852
8. Lasjerdi H, Nasiri-Gheidari Z, Tootoonchian F (2020) Online static/dynamic eccentricity fault diagnosis in inverter-driven electrical machines using resolver signals. IEEE Trans Energy Convers 35(4):1973–1980. https://doi.org/10.1109/tec.2020.2996011
9. Varatharajan A, Pescetto P, Pellegrino G (2020) Sensorless synchronous reluctance motor drives: a full-speed scheme using finite-control-Set MPC in a Projection Vector Framework. IEEE Trans Ind Appl. https://doi.org/10.1109/TIA.2020.2990834
10. Ebrahimi BM, Etemadrezaei M, Faiz J (2011) Dynamic eccentricity fault diagnosis in round rotor synchronous motors. Energy Convers Manage 52(5):2092–2097
11. Ilamparithi TC, Nandi S (2012) Detection of eccentricity faults in three-phase reluctance synchronous motor. IEEE Trans Ind Appl 48(4):1307–1317

12. Naderi P (2015) Eccentricity fault diagnosis and torque ripple analysis of a four-pole synchronous reluctance machine in healthy and faulty conditions. Electric Power Comp Syst 43(11):1236–1245
13. Safa HH, Ebrahimi M, Zarchi HA, Abshari M (2017) Eccentricity fault detection in permanent magnet synchronous generators using stator voltage signature analysis. Int J Precis Eng Manuf 18(12):1731–1737
14. Alani M, Degano M, Bianchi N, Mahmoud H, Gerada C (2021) Analysis and design of dual-rotor synchronous reluctance machine. IEEE J Emerg Select Tops in Power Electronics 9(4):4376–4383
15. Pillai KPP, Nair AS, Bindu GR (2008) Unbalanced magnetic pull in train-lighting brushless alternators with static eccentricity. IEEE Trans Veh Technol 57(1):120–126
16. Safa HH, Zarchi HA (2021) A non-linear model for the rapid prediction of the magnetic field in eccentric synchronous reluctance machines. IEEE Trans Transp Electrif 7(3):1370–1378
17. Fan Y, Cui R, Zhang A (2020) Torque ripple minimization for interturn short-circuit fault based on open-winding five phase FTFSCW-IPM motor for electric vehicle application. IEEE Trans Veh Technol 69(1):282–292
18. Zeraoulia M, Benbouzid MEH, Diallo D (2006) Electric motor drive selection issues for HEV propulsion systems: a comparative study. IEEE Trans Veh Technol 55(6):1756–1764
19. Faiz J, Ebrahimi BM, Akin B, Toliyat HA (2009) Comprehensive eccentricity fault diagnosis in induction motors using finite element method. IEEE Trans Magn 45(3):1764–1767
20. Salah AA, Dorrell DG, Guo Y (2019) A review of the monitoring and damping unbalanced magnetic pull in induction machines due to rotor eccentricity. IEEE Trans Ind Appl 55(3):2569–2580
21. Safa HH, Ebrahimi M, Davoudi A, Pouramin A (2014) Analytical derivation of induction motors inductances under eccentricity conditions. Prog Electromagn Res B 60:95–110
22. Mahmoud H, Bianchi N (2015) Eccentricity in synchronous reluctance motors—part I: analytical and finite-element models. IEEE Trans Energy Convers 30(2):745–753
23. Mahmoud H, Bianchi N, Degano M, Al-Ani M, Gerada C (2018) Eccentric reluctance and permanent magnet synchronous machines comparison. IEEE Trans Ind Appl 54(6):5760–5771
24. Maroufian SS, Pillay P (2018) Torque characterization of a synchronous reluctance machine using an analytical model. IEEE Trans Transp Electrif 4(2):506–516
25. Al-Nuaim NA, Toliyat H (1998) A novel method for modeling dynamic air-gap eccentricity in synchronous machines based on modified winding function theory. IEEE Trans Energy Convers 13(2):156–162
26. Moreira JC, Lipo TA (1992) Modeling of saturated AC machines including air gap flux harmonic components. IEEE Trans Ind Appl 28(2):343–349. https://doi.org/10.1109/28.126740
27. Pal RSC, Mohanty AR (2021) A simplified dynamical model of mixed eccentricity fault in a three-phase induction motor. IEEE Trans Ind Electron 68(5):4341–4350